



Covalently interconnected layers in g-C₃N₄: Toward high mechanical stability, catalytic efficiency and sustainability

Raj Sekhar Roy^{a,1}, Sanjit Mondal^{a,1}, Samita Mishra^a, Maqsuma Banoo^a, Lipipuspa Sahoo^a, Amit Kumar^a, C.P. Vinod^b, Arijit K. De^a, Ujjal K. Gautam^{a,*}

^a Department of Chemical Sciences, Indian Institute of Science Education and Research (IISER)- Mohali, Sector 81, Mohali, SAS Nagar, Punjab 140306, India

^b Catalysis and Inorganic Chemistry Division, CSIR-NCL, Pune 411008, India

ARTICLE INFO

Keywords:

g-C₃N₄
Layer-linkers
Sustainable synthesis
Transient absorption spectroscopy
Water-splitting

ABSTRACT

The grim prospects for the industrial utilization of g-C₃N₄ nanosheets arise from multi-step processing resulting in low material yields and poor visible light response due to quantum confinement. Herein, we introduce a strategy for linking the adjacent layers of g-C₃N₄ covalently to realize a high surface area without excess mass loss in a one-step process by introducing diethylene glycol as a precursor that produces -(CH₂)₂-O-(CH₂)₂- linkers in-situ. Their presence increases interlayer spacing and introduces surface curvatures, discouraging the stacking of a larger number of layers to produce nanosheets with ~3 times higher surface area. Interestingly, unlike other layered materials, the linkers also provide extraordinary mechanical stability against exfoliating forces. In addition, the process instills sub-bandgap states and a considerable visible light response at 500 nm to slow down the picosecond exciton recombination dynamics, resulting in ~5 times enhancement in H₂ generation efficiency from photocatalytic water-splitting over the bulk sample.

1. Introduction

The generation of green hydrogen from photocatalytic water splitting has gained tremendous research interest to alleviate the many problems associated with the increasing use of conventional energy resources, leading to the development of a large number of photoactive materials [1–8]. Among them, the metal-free graphitic carbon nitride (g-C₃N₄) nanostructures are one of the most sought-after photocatalytic materials not only because these are non-toxic, easily preparable, inexpensive, and robust under photocatalytic conditions [9–12], but also due to their high efficiencies for light-harvesting and H₂ generation capabilities. Past research has led to further improvement strategies in their photocatalytic efficiencies that can be broadly classified as (i) improving light-harvesting strategies (since they are usually active for $\lambda < 450$ nm only) [13–18], (ii) improving mass-transfer by surface area engineering [19–24], and (iii) enabling superior excitonic charge separation strategies such as doping or combining with other materials, etc [25–33].

One of the greatest advantages of g-C₃N₄ over most conventional photocatalysts, which can also be a serious disadvantage during their

utilization in real-world applications, is the possibility of easily creating larger surface areas and hence a larger number of catalytically active sites. g-C₃N₄ has a layered structure where the layers are weakly bound to each other enabling their exfoliation to achieve high surface area from the as-prepared bulk samples. Two such strategies are in practice: (i) thermally induced exfoliation where the as-prepared samples are treated at a high temperature. The thermal energy is sufficient to set the layers apart, yielding g-C₃N₄ nanosheets (NS) with a high surface area, and (ii) exfoliation in a liquid media, usually carried out close to room temperature, where ions/molecules get inserted inside the layers to drive them further apart and making them weakly bound so that a further mechanical agitation leads to the separation of the layers to realize a high surface area. However, reducing the layers increases their band gap and further impedes light-harvesting properties. In addition, for large-scale applications, the exfoliation process has certain major disadvantages. Table 1 (which is extended in Table S1) summarizes the usual exfoliation yields in the two approaches. The thermal processes are simpler, but the yields of the nanosheets are even lesser than 10%. On the other hand, liquid-assisted exfoliation processes can give higher yields but have to use an elaborate second step involving chemicals such

* Corresponding author.

E-mail addresses: ujjalgautam@iisermohali.ac.in, ujjalgautam@gmail.com (U.K. Gautam).

¹ These authors contributed equally

as acids that are difficult to handle at a larger scale [20,34]. Exfoliation processes also take longer than the synthesis process itself. Moreover, the optimal solvent to g-C₃N₄ weight ratios are ~1000, making the collection of the exfoliated product a difficult challenge [35].

Therefore, with the motivation of developing a simpler, weight-loss-free strategy for realizing high surface area g-C₃N₄ NSs, we have explored the modification of the bulk synthesis process by introducing reagents that may potentially form adducts with melamine and link the adjacent layers. Not only did we succeed in doing so, but also, we found an additional advantage of superior light harvesting.

Herein, we show that the controlled addition of diethylene glycol (DEG) to melamine, during the conventional single-step bulk synthesis, increases the surface area of the resultant g-C₃N₄ by over three times (21 m²/g), without compromising the product yield. DEG introduces -(CH₂)₂-O-(CH₂)₂- linkers between the adjacent C₃N₄ layers that induce an expansion of the interlayer spacing and limits the stacking stabilization of the layers to yield thinner nanosheets with a high surface area. The linkers however hold the layers together to arrest mass loss during calcination. At the same time, the process enhances the response of the nanosheets to visible light by creating carbon-excess defects that result in an effective uplifting of the valence band, population excess of excitons, and slower exciton recombination dynamics. These nanosheets exhibit 6 times enhancement in photocatalytic hydrogen evolution reaction (HER) activity under visible light irradiation compared to bulk g-C₃N₄. Our findings show the possibility of gross simplification of the synthesis procedure to simultaneously achieve high surface area g-C₃N₄ and extended visible light-harvesting for sustainable hydrogen generation.

2. Experimental section

2.1. Materials synthesis

2.1.1. Synthesis of bulk g-C₃N₄ (CB-B)

The synthesis of bulk g-C₃N₄ was realized following a literature procedure using melamine as precursor materials.[34] Typically, melamine (3 g) was taken in an alumina boat and heated in a tube furnace to 520 °C at a heating rate of 2 °C/min and held for 4 h under aerobic atmosphere. Yellow colored powder of bulk g-C₃N₄ so obtained was then ground using a mortar and pestle, which was washed with water and ethanol followed by drying at 60 °C overnight. For comparison, another bulk g-C₃N₄ sample was prepared under argon atmosphere (CN-A).

2.1.2. One-step synthesis of high surface area g-C₃N₄ (CN-DEG)

The sample was synthesized by a one-step calcination route using a mixture of melamine and diethylene glycol as starting materials. Typically, melamine (3 g) was mixed with diethylene glycol (1 ml) by using a mortar and pestle to prepare a slurry. Next, the slurry was transferred onto an alumina boat and placed in a tube furnace that was heated in an identical fashion as that for bulk g-C₃N₄ under argon atmosphere. Brown colored powder so obtained was then ground using a mortar and pestle to recover a fine powder, which was washed with water and ethanol followed by drying at 60 °C overnight.

Table 1

The key features of the existing exfoliation strategies to realize high surface area g-C₃N₄. (NA: Not applicable. An extended description in Table S1).

Post Synthesis Multistep Processes						
	Sl. No.	Exfoliation Strategy	Time	Yield	Chemicals/ Solvents Used	Collection Process
g-First Step: Synthesis of bulkC ₃ N ₄	1)	Thermal	2 h	6 %	NA	Washing & centrifugation Washing &/or only centrifugation
	2)	Chemical	14 h	60 %	Conc. H ₂ SO ₄	
	3)	Liquid-exfoliation	16 h	100 % at 0.1–0.2 mg/ml scale	H ₂ O/IPA/ NMP/Acetone	

2.2. Photocatalytic H₂ evolution reaction

The photocatalytic activity for hydrogen evolution was evaluated under visible light irradiation. Photocatalytic H₂ evolution reactions were carried out in a 50 ml air-tight top-irradiation glass vessel using an aqueous dispersion of the catalyst. A typical reaction was performed by dispersing g-C₃N₄ (10 mg) powder in water (30 ml) containing 10 vol% triethanolamine (TEOA) as a sacrificial reagent. In the case of deposition of Pt, an appropriate amount of H₂PtCl₆ was dissolved in the reactant solution. The reactant solution was purged with N₂ gas for 1 h to remove air completely before irradiation under a 400 W Xe-lamp fitted with an IR filter to remove the heat component. The wavelength of the incident light was controlled by using an appropriate cut-off filter or band-pass filter. The evolved gases were analyzed by gas chromatography fitted with a TDC detector. The experimental error in the rate of H₂ evolution was within 13 %. The recyclability of the samples was checked under similar experimental conditions. After completing the first cycle, the reaction vessel was thoroughly purged with nitrogen for 1 h, without further adding either sacrificial agent or co-catalysts.

2.3. Transient absorption (TA) Spectroscopy measurements

A pump pulse centered on 400 nm was used to excite all the samples for TA experiments, and a broadband probe pulse with a time delay interrogated the primarily photoexcited samples. The details of the customized femtosecond transient absorption set-up (TAS, Newport) can be seen elsewhere [36,37]. For the generation of 400 nm pump and white light probe, ultrashort pulses centered on 800 nm with pulse width ~54 fs at 1 kHz repetition rate from an amplified Ti: sapphire system (Libra, Coherent) was used. We have used a type-1 beta-barium borate crystal (0.2 mm thick), which generates the second harmonic of 800 nm pump pulse and we obtained the pump pulse centered at 400 nm. Part of the same Ti: sapphire laser output was used to produce the broad white-light probe by pumping a CaF₂ crystal. For all the samples, differential absorption spectra (obtained by blocking alternate pump pulses) were collected by varying the pump-probe time-delay keeping 5 s integration time (i.e. averaging over 5000 laser shots).

All the pump-probe decay time traces data were fitted using the Gaussian convolution with exponential decay equation (Eq. 1) using standard deviation (σ) as 0.1 ps and plotted using Matlab programming (Mathworks Inc). Gaussian deconvolution method already identified the time-zero and the raw data is time-shifted accordingly, for each time traces [38].

$$y(t, \sigma, \mu, \tau) = \sum_{i=1}^3 \alpha_i \left(\frac{1}{2\tau_i} \right) \text{Exp} \left(\frac{1}{2\tau_i} (2\mu + \frac{\sigma^2}{\tau_i} - 2(t - t_0)) \right) \text{erfc} \left[\frac{(\mu + \frac{\sigma^2}{\tau_i} - (t - t_0))}{\sigma\sqrt{2}} \right] \quad (1)$$

where, A is the background term, τ_i are the decay time with corresponding amplitudes α_i and μ is the mean and σ is IRF/2.33.

3. Results and discussion

The as-prepared g-C₃N₄ sample in the presence of DEG (CN-DEG) has shown two stark differences, firstly in color as compared to conventional g-C₃N₄ samples, appearing brownish, and indicating the absorption of a much larger fraction of the visible radiation (photographs as insets in Fig. 1a). Second, it exhibited remarkable mechanical stability due to the presence of covalent linkers between the adjacent carbon nitride layers, as explained vide infra. Notably, the yields of the reaction product with respect to melamine precursors were identical for both the samples within a $\pm 2\%$ deviation (Fig. 1a).

3.1. Single-step realization of high surface area (SA)

Several tools were employed to compare the properties of CN-DEG and the conventional g-C₃N₄. The powder X-ray diffraction (XRD) analysis of the samples (Fig. 1b) shows two prominent peaks at $\sim 13^\circ$ and $\sim 27^\circ$ corresponding to the in-plane repetition of the heptazine units in the (100) plane and the interlayer distances along (002) planes respectively. There are, however, two differences: i) a noticeable decrease in the (002) peak intensity in CN-DEG when normalized with the (100) peak intensity, indicating thinner sheets or poorer crystallinity along the (002) axis, and ii) a shift in the peak maximum of the (002) peak from 27.3° to 27.1° in the CN-DEG sample indicating expansion of the layer spacings. It may be noted that the expansion in layer spacings need not be predictable based on the size of the linkers because DEG moieties will possibly be at some non-orthogonal angles with respect to the basal planes. Each of the four sp^3 C atoms in the linkers offers a possibility of deviating from a simple orthogonal interconnection. The FTIR spectra of CN-B and CN-DEG (Fig. S1) revealed similar features with broad peaks between 2900 and 3400 cm^{-1} corresponding to the N-H bonds of uncondensed residual amino groups [39,40], whereas the peaks in the $1200\text{--}1730\text{ cm}^{-1}$ range originate from the heptazine-derived repeating units, and the peak at 805 cm^{-1} arises due to triazine-ring [41]. The absence of any noticeable feature in the FTIR spectra suggests that DEG, if incorporated into the bare g-C₃N₄ structure,

ought to be in very minute quantities and keeping the core heptazine moiety of C₃N₄ intact. The transmission electron microscopy (TEM) and scanning electron microscopy (SEM) images of CN-B and CN-DEG are displayed in Fig. 1c, d and Fig. S2 respectively. A thorough TEM imaging of the CN-B sample shows sheets that appear flat (probably rigid) and semi-transparent to the electron beam, indicating good crystallinity. TEM images on the CN-DEG sample, on the other hand, indicate the presence of thinner sheets that appear more transparent and significantly defective as inferred from their highly and randomly curved surfaces.

To verify the underscoring effects, the specific surface areas of these samples were analyzed (Fig. 2a). CN-DEG has a specific SA of $21.0\text{ m}^2\text{ g}^{-1}$, which is ~ 3 times higher than that of CN-B ($7.1\text{ m}^2\text{ g}^{-1}$) suggesting that the CN-DEG sample indeed contains thinner nanosheets. Besides a higher SA, the corrugated CN-DEG sheets also exhibit 3 times enhancement in porosity, desirable for facile mass transfer during their use in catalytic processes. Pore size distribution in CN-DEG (inset of Fig. 2a) depicts the increase in the number of the regular pores of carbon nitride structure and also the opening of new pores with higher pore size. Thus, considering the production of similar quantities of products, the addition of DEG resulted in high surface area C₃N₄ in a single step without compromising the reaction yield, which is in contrast to conventional approaches of thermal and chemical exfoliation where not only the yields are compromised, but the processes are also significantly complicated, especially for scale-up production.

3.2. Remarkable mechanical stability of CN-DEG

While exploring the role of DEG in CN-DEG, an unexpected phenomenon of high mechanical stability of the sample was discovered that we subsequently related with the linking of the adjacent C₃N₄ layers potentially with $-(\text{CH}_2)_2\text{-O-(CH}_2)_2-$ moieties derived in-situ from DEG, which is also supported by the variation of the layer distances observed in the XRD analysis and the excess of $-sp^3$ carbon observed in XPS analysis. We subjected the CN-DEG sample to prolonged bath-sonication expecting further improvement in surface area. By analyzing the entire

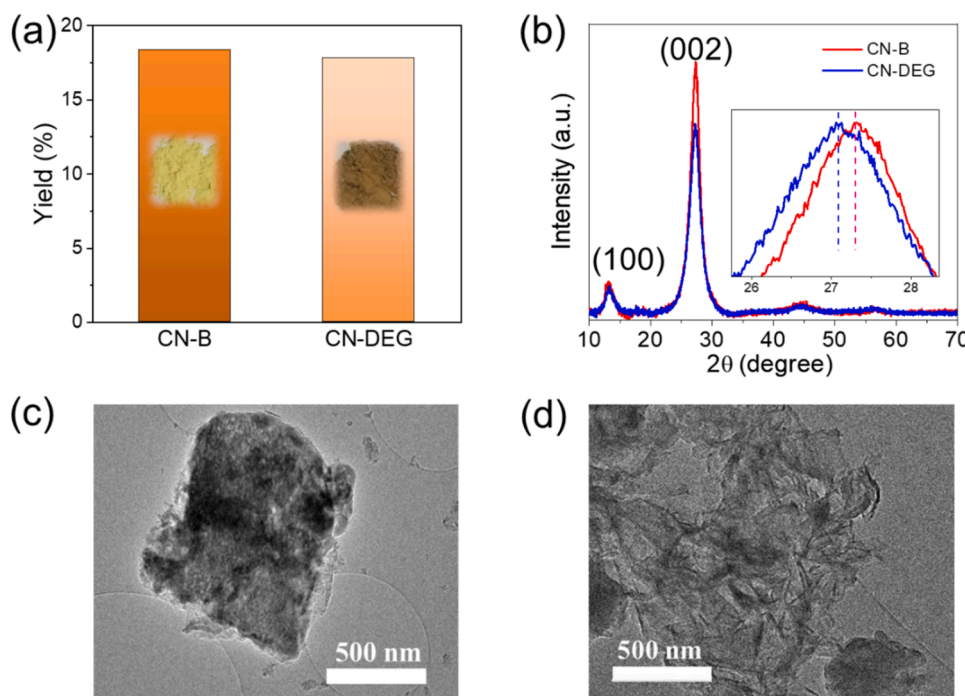


Fig. 1. (a) Comparison between production yields of CN-B and CN-DEG (insets shows the photographs of CN-B and CN-DEG), (b) XRD patterns of CN-B and CN-DEG (Inset shows a shift in the peak maximum of the (002) peak in the CN-DEG sample indicating shrinkage of the layer spacings). TEM images of CN-B (c) and CN-DEG (d).

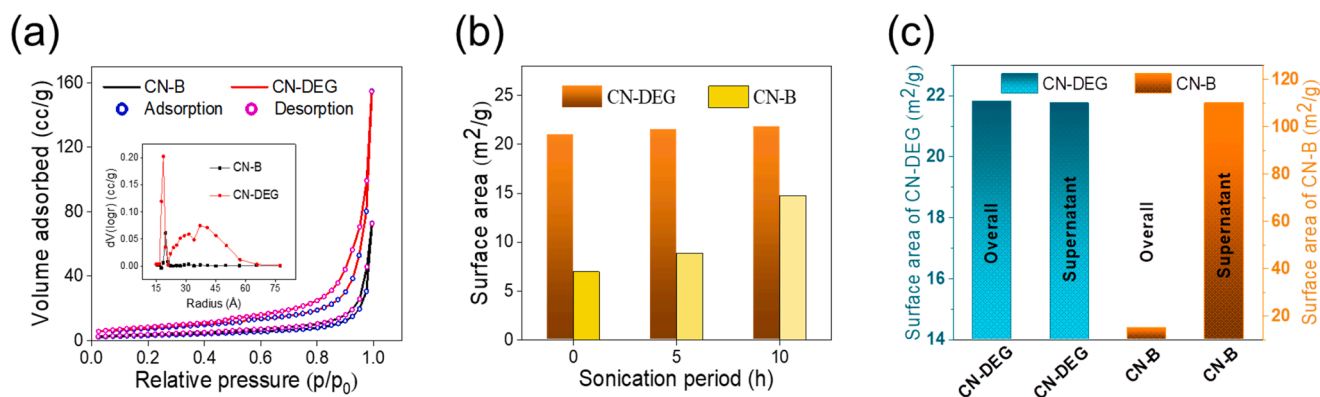


Fig. 2. a). N₂ adsorption-desorption isotherms for CN-B and CN-DEG samples (inset shows pore size distribution). (b) Variation in surface area of CN-B and CN-DEG upon ultrasonication for different time periods. (d) Surface area of total recovered sample and supernatant of the dispersion of CN-B and CN-DEG after sonication.

sample after sonication for 5 h and 10 h, as shown in Fig. 2b, we observed barely any change in the SA. The enhancement in SA after 10 h is only 6 % (21.8 m² g⁻¹), indicating that the layers cannot be separated, while the same for CN-B was ~30 % (8.9 m² g⁻¹) even after 5 h and ~110 % (14.8 m² g⁻¹) after 10 h of similar treatment. On the other hand, when we analyzed only the top, floating portion of the sample after resting the sample post-sonication dispersion for ~10 min, allowing the heavier particles to settle down, the SA of the CN-DEG sample remained the same while the CN-B sample acquires a SA of > 100 m² g⁻¹ (~1500 % increase, but in rather low yields, as observed widely [34] (Fig. 2c. and Fig. S3).

Thermogravimetry analysis (TGA) also showed that the weight loss of the CN-DEG sample occurs at a higher temperature. As shown in Fig. S4, significant weight loss initiates at 475 °C for CN-B while the same starts only at 520 °C for CN-DEG. Similarly, 50 % weight loss was

observed at 645 °C for CN-B while the same occurred at 685 °C for CN-DEG. Interestingly, the CN-B sample completely disappears at 715 °C while the heat treatment of CN-DEG leaves behind a small quantity of the sample in the TGA pan even at 900 °C. A TEM image of the left-over sample from the TGA treatment of CN-DEG is shown in the inset of Fig. S4. Heating of DEG alone results in complete evaporation at much lower temperatures. Therefore, we attribute the recovery of the small fraction of the sample to the excessively interconnected C₃N₄ layers which do not at all get thermally exfoliated which is necessary for mass loss.

3.3. Linking of adjacent C₃N₄ layers in CN-DEG

The tremendous tailoring of the SA, porosity, and surface texture from the simple addition of DEG during g-C₃N₄ synthesis is augmented

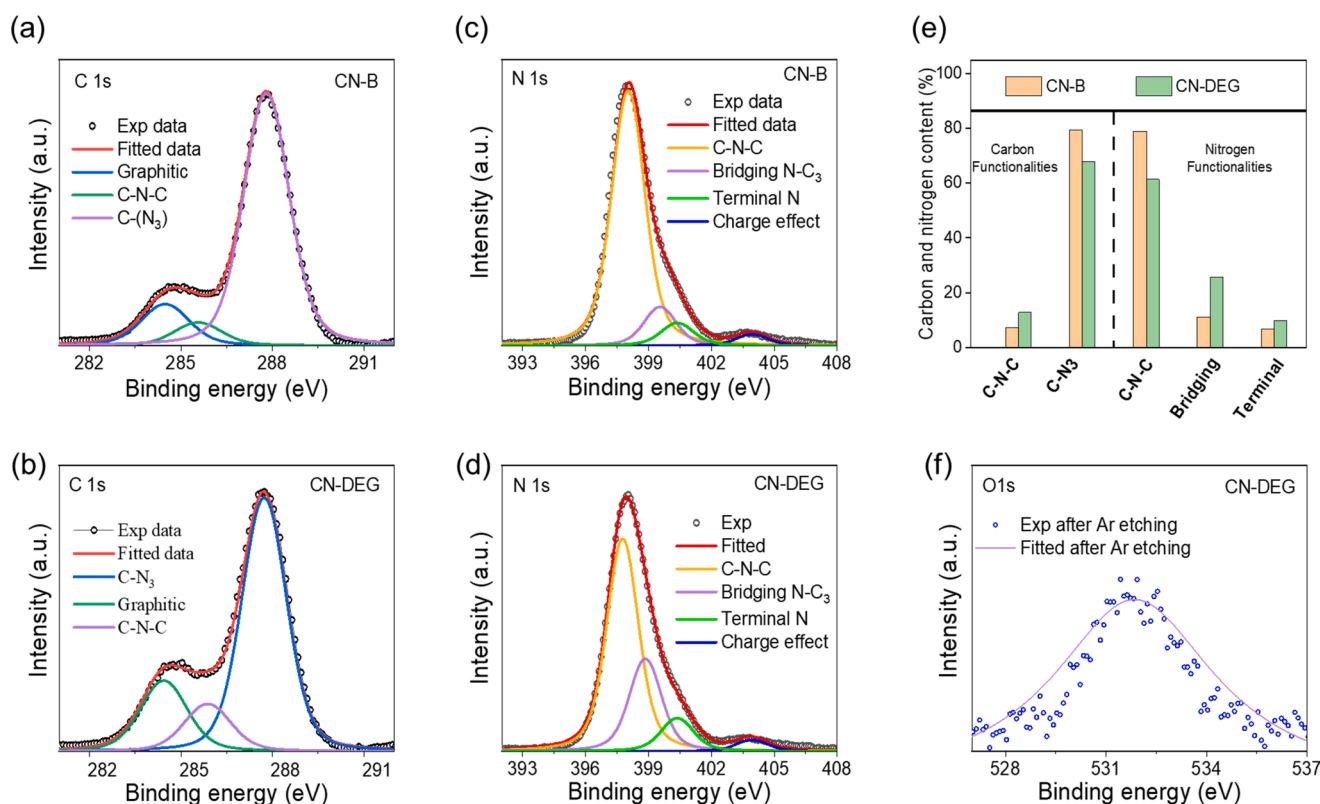


Fig. 3. High resolution of (a, b) C 1s XPS spectra of CN-B and CN-DEG; and (c, d) N 1s XPS spectra of CN-B and CN-DEG respectively. (e) Plot showing relative abundance of C and N in different environments in CN-B and CN-DEG. (f) High resolution O 1s spectrum after Ar etching of the sample.

by the compositional changes as observed from the X-ray photoelectron spectroscopic (XPS) study (Fig. S5). The high-resolution C 1s spectra (Fig. 3a, b), contains three peaks at binding energies of 284.4, 285.6, and 287.8 eV respectively. The 285.6 and 287.8 eV peaks can be attributed to the sp^2 C-atoms bonded to the nitrogen in an aromatic ring (C-N-C) and sp^2 -hybridized carbon in the aromatic ring attached to the bridging and terminal NH_2 group (C-(N)₃) respectively. [34] The peak at 284.4 eV is graphitic carbon [34]. The N 1s spectra of both the samples appear identical. As seen in Fig. 3c, d, the spectra consists of three peaks at binding energies 397.5, 398.9, and 400.1 eV that are ascribed respectively to ring nitrogen (C-N-C), bridging nitrogen (N-(C)₃) of heptazine units, and terminal nitrogen (N-H) present at the edges as unpolymerized moieties of CN-B [34].

The similarity between the XPS spectra of the two samples establishes the presence of such surface functionalities that resembles bare g-C₃N₄. However, there is an apparent increase in peak area corresponding to the peak of C-N-C in the C spectrum of CN-DEG than CN-B (Fig. 3e), which we attribute to the presence of sp^3 carbons originating from DEG moieties as the binding energies of ring carbon (C-N-C) present in heptazine rings and sp^3 -C domains match extremely closely. [42] Notably, an increase in the C/N ratio in CN-DEG by ~5% in comparison to bulk g-C₃N₄ from CHN analysis is consistent with the presence of excess carbon from linkers in the CN-DEG sample. On the other hand, C-N-C component of N decreases in CN-DEG while the same in the bridging position increases, suggesting the presence of excessive pores in the structure which originate due to poor polymerization around the N moieties connected to the linkers.

In addition, we have also recorded the O-1s high-resolution spectrum in the CN-DEG sample after Ar etching to clean the surface (details in Fig. S6, [43,44]). Therein, the presence of oxygen peak (Fig. 3f) indicates the incorporation of DEG moieties at the bridging sites or the edges. Nonetheless, the extra stability of CN-DEG under sonication and its lattice expansion encourages us to suggest the presence of DEG-derived moieties in the sample as linkers.

Based on XRD, TGA, XPS analysis, and surface area variation under exfoliation conditions, a plausible scheme describing the various

reactions involved in the synthesis and the structure of the product is given in Fig. 4. Accordingly, adducts are initially formed resulting from a condensation reaction between melamine and DEG, quenching either one or both the terminal alcoholic group. Only some of the terminal amines will undertake this reaction due to limited mass transfer under the synthesis conditions while the other melamine molecules will produce heptazine.

Subsequently, the excess triazine moieties and the adducts undergo polymerization to yield heptazine moieties attached with the DEG-derived linkers. Finally, C₃N₄ sheets grow involving those heptazine moieties attached with the linkers as well as free heptazine and triazine moieties. The sp^3 -atoms present in the $-(CH_2)_2O-(CH_2)_2-$ linkage brings non-planarity to the structure and therefore the two heptazine moieties across the linkage can become part of two adjacent growing C₃N₄ layers, thus covalently linking them. The lattice expansion in the presence of the linkers, as observed in XRD analysis, reduces the layer adhesion forces and prompts the formation of eventually thinner g-C₃N₄ sheets with higher surface area, wherein lattice defects also induce porosity. A possibility of DEG-Melamine adduct formation was established by controlled adduct formation and a series of control experiments provides evidence for the proposed structure shown in Fig. 4b (details in Supplementary Note 2 & 3, Fig. S7 and Fig. S8).

3.4. Optical properties and femtosecond charge-transfer dynamics

The deep yellow color of the CN-DEG sample is counter-intuitive since thinner sheets should exhibit, at best, a blue-shifted absorption [19]. To elucidate the effect of the structural modifications in CN-DEG, we investigated their optoelectronic properties in detail. The UV-Vis diffuse reflectance spectra (DRS) of the two samples (Fig. 5a) show that CN-B, as expected, exhibits an adsorption onset at ~500 nm, while the absorption tail of the CN-DEG sample extends beyond 550 nm, implying a significantly improved visible light response. The prominent Urbach tail in the case of CN-DEG is indicative of the presence of sub-bandgap defect states [45], which were confirmed as shallow trap-states from transient absorption spectroscopy (TAS) as discussed

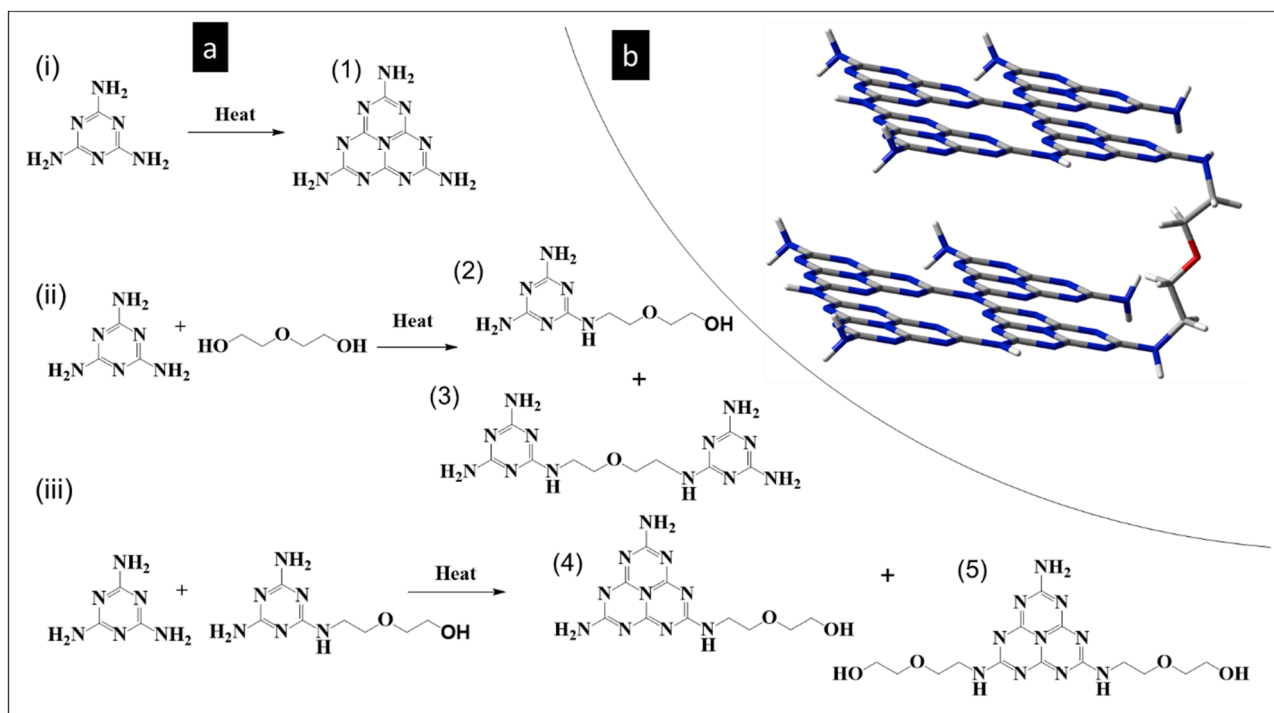


Fig. 4. (a) Scheme showing various possible reactions and products formed as intermediates during the synthesis of CN-DEG. (b) Schematic showing two C₃N₄ layers interconnected by a DEG derived $-(CH_2)_2O-(CH_2)_2-$ linker.

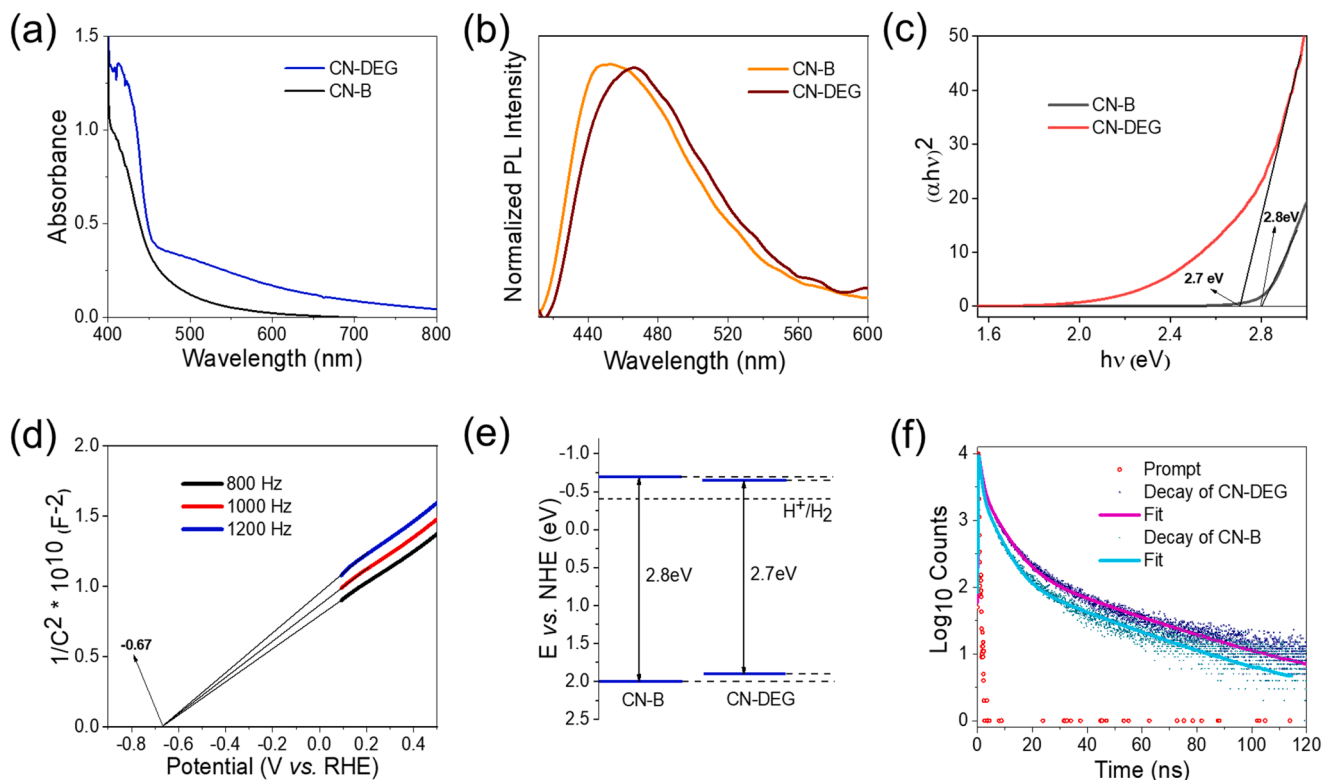


Fig. 5. (a) Diffuse reflectance spectra and (b) normalized PL spectra of CN-B and CN-DEG. (c) Corresponding Tauc plot derived from the DRS plot. (d) Mott-Schottky plots of CN-DEG. (e) Schematic of relative band alignment of CN-B and CN-DEG. (f) Time-resolved photoluminescence decay kinetics plot from TCSPC measurement upon excited with a 375 nm laser.

later. Similarly, the photoluminescence (PL) spectrum of CN-DEG also showed a red-shifted asymmetric emission band centered (λ_{em}) at 465 nm in comparison to CN-B (λ_{em} ~450 nm) as displayed in Fig. 5b.

The bandgaps of CN-B and CN-DEG were estimated as ~2.8 and ~2.7 eV respectively from the corresponding Tauc plots (Fig. 5c). The conduction band (CB) edges of both the samples were determined by Mott-Schottky measurement (Fig. 5d, Fig. S9). [46–50] Accordingly, Fig. 5e summarizes the band alignment of CN-B and CN-DEG with respect to the proton reduction potential. The decrease in the bandgap of CN-DEG compared to CN-B is contributed by both the uplifting of the valence band (VB) edge of CN-DEG, which we attribute to the fall in abundance of electronegative nitrogen atoms contributing to the VB and the stabilization of the CB because of incorporation of excess carbon. [51, 52].

The deconvolution of the broad PL spectra yielded two peaks at 446 nm (~2.78 eV) and 482 nm (2.57 eV) for CN-B and 455 nm (2.73 eV) and 488 nm (2.54 eV) for CN-DEG (Fig. S10). The bands centered on ~2.7 eV suggest that the high-energy PL emission is close to the bandgap, indicating the presence of additional emissive intra-bandgap states roughly 0.2 eV below the absorption band boundaries. [53] For the case of CN-B the emission at 450 nm most likely corresponds to the recombination between π^* and LP states and the emission at 488 nm to π^* and π states [34]. The average lifetime of the excited electrons was analyzed by time-resolved spectroscopy using time-correlated single photon count (TCSPC) measurements and the decay plots (Fig. 5f) were fitted to a triple-exponential function (Table 1) using the formula:

$$\text{Average lifetime } (\tau) = \frac{\tau_1 A_1 + \tau_2 A_2 + \tau_3 A_3}{A_1 + A_2 + A_3}$$

where, τ_1 , τ_2 , and τ_3 represent emission lifetimes in three different time stages and A_1 , A_2 , and A_3 represent the amplitude of different emission lifetimes, as given in Table 2. These lifetime components show the

Table 2

Time-components and related amplitudes of fitting of TCSPC decay for CN-B and CN-DEG obtained after 375 nm laser excitation.

Sample	A_1	τ_1 (ns)	A_2	τ_2 (ns)	A_3	τ_3 (ns)	X^2	$\langle \tau \rangle$ ns
CNB	0.41	1.9	0.09	6.4	0.50	0.46	1.09	1.60
CN-DEG	0.40	2.11	0.08	7.74	0.52	0.56	1.12	1.75

emission through different relaxation channels. The average emission lifetime (τ) of the CN-B (~1.69 ns) is shorter than the CN-DEG (~1.78 ns) and is attributed to the enhanced contribution from trap-assisted slow recombination in CN-DEG.

We have studied the effect of band-tailoring in optical properties using femtosecond transient absorption (TA) spectroscopy to reveal ultrafast excited-state relaxation dynamics not captured by time-resolved photoluminescence study. We have excited both samples using a 400 nm pump and white light as a probe. [36,37] CN-B exhibited a broad negative signal with a maximum at 505 nm which is due to the contribution of both ground-state bleaching (GSB) and stimulated emission (SE) (Fig. 6a). Similarly for CN-DEG, the broad negative signal with a maximum at 505 nm is also due to the contribution from both GSB and SE (Fig. 6b). To compare the relaxation dynamics for CN-B and CN-DEG, we have fitted the kinetic traces at 505 nm. For CN-B, the best-fitting was found by using a bi-exponential where the shorter component (20 ps) corresponds to intraband vibrational relaxation and the longer component (2.1 ns) originating from charge recombination. On the other hand, the kinetic traces for CN-DEG at 505 nm was found to be best fitted using a tri-exponential where the shortest component (8.5 ps) corresponds to the intraband vibrational relaxation and the other short component (770 ps) is the trap-assisted component, while the long component (6.1 ns) corresponds the charge recombination (Fig. 6c, d).

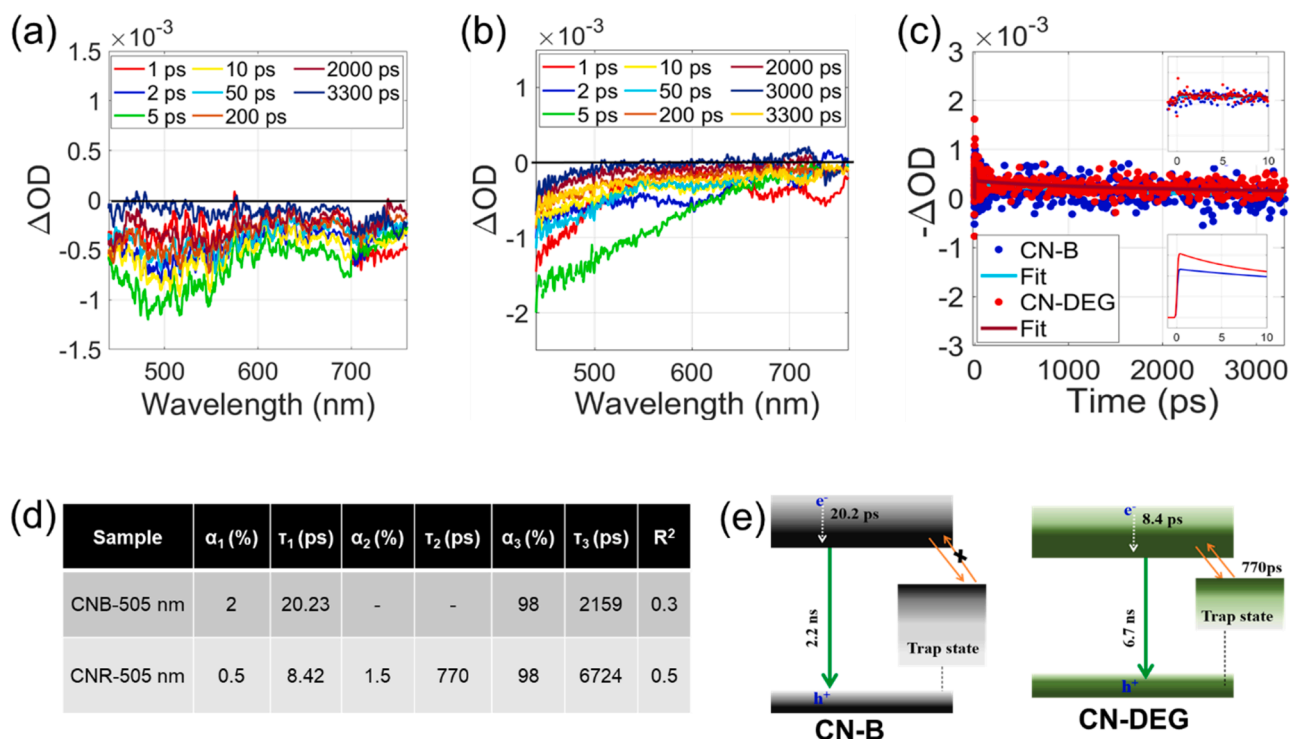


Fig. 6. Spectral traces at the different pump-probe delay for a) CN-B, b) CN-DEG; c) Kinetic traces for CN-B and CN-DEG at 505 nm, (d) Time-components and related amplitudes of CN-B and CN-DEG at 505 nm wavelength obtained after 400 nm excitation. (e) Schematic for the photoluminescence pathways.

These assignments are based on the earlier observation that the lifetime for deep trap states is much longer (μs) compared to shallow trap states (ps) [53]. This is why we observe the trap-assisted recombination for the case of CN-DEG which has shallow trap states (allowing de-trapping to occur) but not for CN-B for which deep trap states exist.

Since the bandgap of CN-DEG is less than that of CN-B, so the nature of its trap states is also different where the trap states lie near the band edge to make trapping and de-trapping easy for CN-DEG, but which is not possible in CN-B (Fig. 6e) [54]. The long component (corresponding to charge recombination) is longer in the case of CN-DEG than that of CN-B

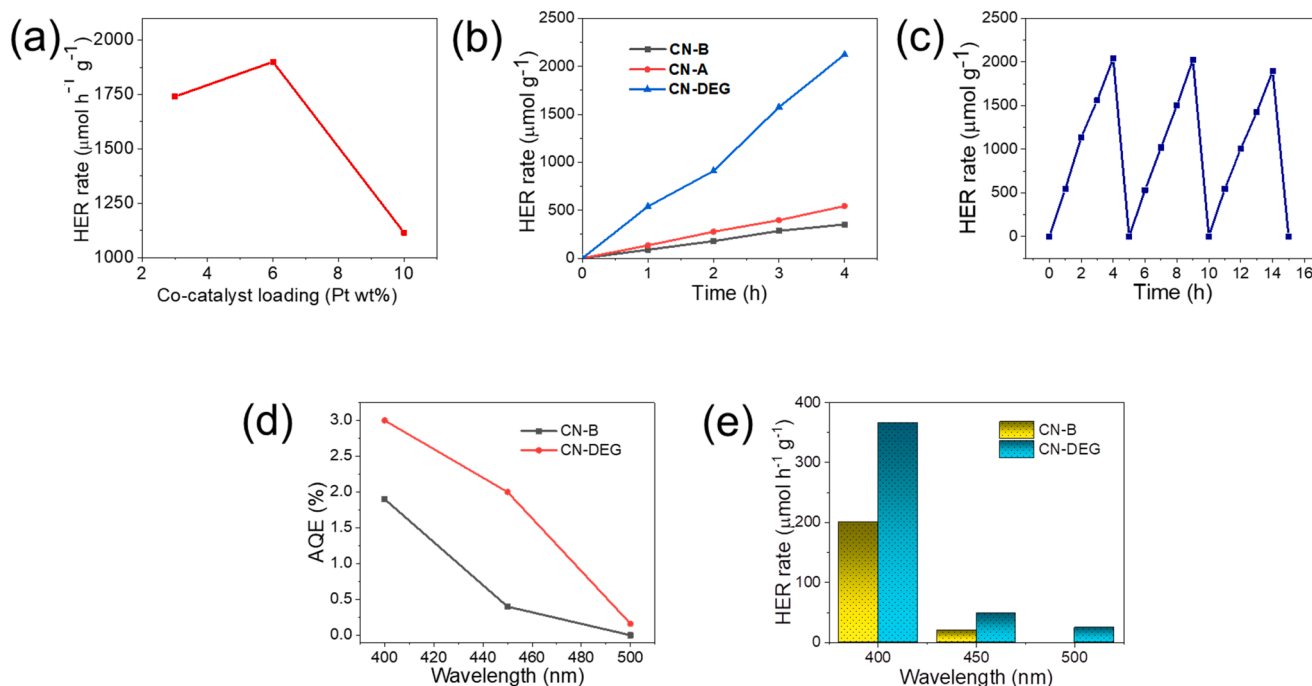


Fig. 7. (a) Effect of co-catalyst loading on CN-DEG sample on H_2 evolution efficiency. (b) H_2 production rate of CN-B, CN-A and CN-DEG in the presence of co-catalyst (6 wt% Pt) and hole scavenger (10 vol% TEOA) under visible-light irradiation (using 420 cut-off filter under a 400 W Xe lamp). (c) Cyclic hydrogen production by CN-DEG over 12 h of visible light illumination. (d) A plot of apparent quantum efficiencies of the samples vs. different incident wavelengths. (e) Hydrogen evolution rate exhibited by CN-B and CN-DEG under different band-pass filters.

due to the fact that trapping and de-trapping of electron retains it in the excited state for a longer time [55]. We, however, rule out the possibility of interband emission from trap states as such emission should be much red-shifted [56].

3.5. Photocatalytic performance

The high surface area, extended visible light response, and slower exciton recombination dynamics coupled with the single-step synthesis prospects for sustainable production inspired the investigations on the use of CN-DEG in photocatalytic hydrogen evolution reaction (HER) from water-splitting. The HER performances were evaluated under the irradiation of a 400 W Xe lamp fitted with a 420 nm cut-off filter, which showed that the CN-DEG sample exhibits a tremendous rate enhancement over the bulk $g\text{-C}_3\text{N}_4$ sample synthesized under similar conditions. We first checked the HER performance by loading different amounts of Pt on CN-DEG (Fig. 7a). The best HER activity was achieved when the Pt loading is 6 wt%, and the same decreases upon further increase in the loading amount. Therefore, 6 wt% Pt loading was used for all HER experiments. Fig. 7b displays the hydrogen evolution rates of the samples showing that the evolution consistently increases with light exposure time. The hydrogen production by CN-DEG is quite facile, with a gas evolution rate of $540 \mu\text{mol h}^{-1} \text{g}^{-1}$ which is 5 times higher than that of CN-B. The photocatalytic HER efficiency using a bare $g\text{-C}_3\text{N}_4$ sample synthesized in Ar atmosphere (CN-A) was also studied in order to check the role of atmosphere in enhancement of photocatalytic activity. We have observed $g\text{-C}_3\text{N}_4$ samples made in argon atmosphere in absence of DEG show comparable HER rate with the same made under Air atmosphere and negligible rate enhancement when compared with CN-DEG. Furthermore, the durability of the catalyst during HER was checked by performing three repeat cycles of 4 h each. Fig. 7c shows that the stability of CN-DEG is excellent with negligible decline (3–5%) after each cycle.

To examine the contribution of the extended light absorption in CN-DEG to its catalytic activity, we have further evaluated wavelength specificity of the photocatalyst. The activities were compared by irradiating the reaction mixture using various band-pass filters with wavelength maxima at 400 nm, 450 nm, and 500 nm, and calculating the apparent quantum efficiencies (AQE, details in Supplementary Note 1). The CN-DEG sample exhibited a rather superior activity under visible light. Fig. 7d,e show the AQEs and the H_2 evolution rates estimated for the two samples. As compared to CN-DEG, the H_2 evolution rate for CN-B is 1.8 and 2.0 times lower at 400 nm (AQEs: 3 and 1.9) and 450 nm (AQEs: 2 and 0.4) respectively. At 500 nm, CN-B showed no activity while the AQE for CN-DEG was estimated to be 0.16, confirming its performance is boosted by a superior visible light response. Note that the photocatalytic activity improvement ratio of the two samples after specific area normalization is 1.66 folds. The extra enhancement in CN-DEG is attributed to improved visible-light absorbance and shallow trap-state assisted increased excitonic lifetime.

Although exfoliated $g\text{-C}_3\text{N}_4$ NSs reported in the literature show somewhat higher activities (5–6 times higher when not used in Z-scheme) than the best efficiencies found in this study, the CN-DEG sample may be considered to have many advantages for industrial utilization. For example, under 300 W Xe lamp, Niu et al. could achieve a higher ($800 \mu\text{mol h}^{-1} \text{g}^{-1}$) HER rate using thermally exfoliated $g\text{-C}_3\text{N}_4$ nanosheets, the yield of the nanosheets are very low (6 %) after the two steps in synthesis.[19] Another study, an even greater enhancement in HER activity ($1860 \mu\text{mol h}^{-1} \text{g}^{-1}$ under 300 W Xe lamp) was observed using $g\text{-C}_3\text{N}_4$ nanosheets obtained in a liquid exfoliation process.[21] Any liquid exfoliation strategy takes 10–16 h of additional time for sonication and also involves a large volume of solvents, as discussed vide-supra.[35] The chemical exfoliation pathways also have limited scope its industrial application because they involve exothermic steps due to the use of acids, and an additional cooling setup is needed [20]. Therefore, introducing linkers between adjacent layers could be an

optimal way of improving the surface area, visible light harvesting, and HER activity of $g\text{-C}_3\text{N}_4$ while limiting the synthesis step to just one and with greater scale-up production prospects. Furthermore, from the TEM images of CN-DEG (Fig. S11a, b) recorded after catalysis, it is observed that there is no apparent change in the sample from that of the fresh material. Similarly, from PXRD pattern (Fig. S11c) of CN-DEG after catalysis, no changes were observed, indicating the stable nature of the material during catalysis.

4. Conclusion

In conclusion, for the sake of sustainability, we introduce a one-step synthesis strategy for the realization of high surface area $g\text{-C}_3\text{N}_4$, but without compromising on the product yield which has invariably been the case while attempting to achieve their high surface area. The key to achieving the same is proposed to be the introduction of linker moieties between the adjacent C_3N_4 layers, which leads to lattice expansion along the layer-stacking direction, thereby decreasing the layer adhesion forces and discouraging the extensive stacking akin to bulk $g\text{-C}_3\text{N}_4$. This effect is farther aided by the introduction of defects in the layers creating prominent surface undulations. Besides, linked $g\text{-C}_3\text{N}_4$ exhibited improved visible light absorption ability up to 500 nm while exfoliated nanosheets generally exhibit blue-shifted optical absorption due to quantum confinement. These novel nanosheets showed 5 times enhancement in H_2 evolution rate under visible light irradiation compared to bulk $g\text{-C}_3\text{N}_4$. The present findings are important as these demonstrate an industry-friendly strategy to simultaneously enhance the visible light response and surface area of a $g\text{-C}_3\text{N}_4$. We believe suitable tailoring of the process can further improve the surface area, yield, and photocatalytic activity by introducing more appropriate linkers.

CRedit authorship contribution statement

Raj Sekhar Roy - Experiment design, data acquisition and curation, validation of the concept, original draft writing; Sanjit Mondal - Experiment design, catalyst synthesis, validation of the concept; Samita Mishra - Experimental design and data collection of optical studies, manuscript review; Maqsuma Banoo - Catalytic experiments, manuscript review; Lipipuspa Sahoo - Experimental setup design; Amit Kumar - Data collection for optical studies, manuscript review; C. P. Vinod - Surface characterization; Arijit K. De- Supervision of optical studies, manuscript writing and reviewing; Ujjal K. Gautam - Supervision, project administration, funding acquisition, manuscript writing and editing.

Declaration of Competing Interest

The authors declare that they have no known competing financial interests or personal relationships that could have appeared to influence the work reported in this paper.

Data Availability

Data will be made available on request.

Acknowledgments

RSR is grateful to MHRD, India, for a senior research fellowship (SRF). SM is grateful to MHRD, India, for a senior research fellowship (SRF). MB is grateful to CSIR, India, for a senior research fellowship (SRF). L.S. thanks UGC (India) for SRF. Authors express their acknowledgment to Sakshi Chawla for assistance during the TAS measurement. We would like to gratefully acknowledge the central (TEM, SEM, PXRD) and departmental (PL, TCSPC) facilities at IISER Mohali. Authors gratefully acknowledge the support from Science and Engineering

Research Board (SERB), India under the grant CRG/2021/001420.

Appendix A. Supporting information

Supplementary data associated with this article can be found in the online version at [doi:10.1016/j.apcatb.2022.122069](https://doi.org/10.1016/j.apcatb.2022.122069).

References

- [1] K. Maeda, K. Domen, Photocatalytic water splitting: Recent progress and future challenges, *J. Phys. Chem. Lett.* 1 (2010) 2655–2661, <https://doi.org/10.1021/jz1007966>.
- [2] D. Ruan, S. Kim, M. Fujitsuka, T. Majima, Defects rich g-C₃N₄ with mesoporous structure for efficient photocatalytic H₂ production under visible light irradiation, *Appl. Catal. B Environ.* 238 (2018) 638–646, <https://doi.org/10.1016/j.apcatb.2018.07.028>.
- [3] S.J.A. Moniz, S.A. Shevlin, D.J. Martin, Z.X. Guo, J. Tang, Visible-light driven heterojunction photocatalysts for water splitting—a critical review, *Energy Environ. Sci.* 8 (2015) 731–759, <https://doi.org/10.1039/c4ee03271c>.
- [4] T. Hisatomi, K. Domen, Reaction systems for solar hydrogen production via water splitting with particulate semiconductor photocatalysts, *Nat. Catal.* 2 (2019) 387–399, <https://doi.org/10.1038/s41929-019-0242-6>.
- [5] S.R. Lingampalli, U.K. Gautam, C.N.R. Rao, Highly efficient photocatalytic hydrogen generation by solution-processed ZnO/Pt/CdS, ZnO/Pt/Cd1-xZnxS and ZnO/Pt/CdS 1-xSex hybrid nanostructures, *Energy Environ. Sci.* 6 (2013) 3589–3594, <https://doi.org/10.1039/c3ee42623h>.
- [6] Y. Wang, L. Liu, T. Ma, Y. Zhang, H. Huang, 2D graphitic carbon nitride for energy conversion and storage, *Adv. Funct. Mater.* 31 (2021) 1–36, <https://doi.org/10.1002/adfm.202102540>.
- [7] Y. Huang, K. Wang, T. Guo, J. Li, X. Wu, G. Zhang, Construction of 2D/2D Bi₂Se₃/g-C₃N₄ nanocomposite with high interfacial charge separation and photo-heat conversion efficiency for selective photocatalytic CO₂ reduction, *Appl. Catal. B Environ.* 277 (2020), 119232, <https://doi.org/10.1016/j.apcatb.2020.119232>.
- [8] X. Feng, R. Zheng, C. Gao, W. Wei, J. Peng, R. Wang, S. Yang, W. Zou, X. Wu, Y. Ji, H. Chen, Unlocking bimetallic active sites via a desalination strategy for photocatalytic reduction of atmospheric carbon dioxide, *Nat. Commun.* 13 (2022) 2146, <https://doi.org/10.1038/s41467-022-29671-0>.
- [9] A. Naseri, M. Samadi, A. Pourjavadi, A.Z. Moshfegh, S. Ramakrishna, Graphitic carbon nitride (g-C₃N₄)-based photocatalysts for solar hydrogen generation: recent advances and future development directions, *J. Mater. Chem. A* 5 (2017) 23406–23433, <https://doi.org/10.1039/c7ta05131j>.
- [10] X. Wang, K. Maeda, A. Thomas, K. Takanabe, G. Xin, J.M. Carlsson, K. Domen, M. Antonietti, A metal-free polymeric photocatalyst for hydrogen production from water under visible light, *Nat. Mater.* 8 (2009) 76–80, <https://doi.org/10.1038/nmat2317>.
- [11] G.Z.S. Ling, S.F. Ng, W.J. Ong, Tailor-engineered 2D cocatalysts: harnessing electron-hole redox center of 2D g-C₃N₄ photocatalysts toward solar-to-chemical conversion and environmental purification, *Adv. Funct. Mater.* 2111875 (2022) 1–33, <https://doi.org/10.1002/adfm.202111875>.
- [12] L. Sun, M. Yang, J. Huang, D. Yu, W. Hong, X. Chen, Freestanding graphitic carbon nitride photonic crystals for enhanced photocatalysis, *Adv. Funct. Mater.* 26 (2016) 4943–4950, <https://doi.org/10.1002/adfm.201600894>.
- [13] D.A. Links, Y. Wang, Y. Di, M. Antonietti, H. Li, X. Chen, X. Wang, L. Jiang, X. Yuan, G. Zeng, J. Liang, Z. Wu, H. Yu, Y. Zhang, T. Mori, J. Ye, M. Antonietti, Carbon self-doping induced high electronic conductivity and, *J. Colloid Interface Sci.* 4 (2010) 17–29, <https://doi.org/10.1016/j.jcis.2018.10.033>.
- [14] G. Zhang, M. Zhang, X. Ye, X. Qiu, S. Lin, X. Wang, Iodine modified carbon nitride semiconductors as visible light photocatalysts for hydrogen evolution, *Adv. Mater.* 26 (2014) 805–809, <https://doi.org/10.1002/adma.201303611>.
- [15] S.A. Shevlin, Z.X. Guo, Anionic dopants for improved optical absorption and enhanced photocatalytic hydrogen production in graphitic carbon nitride, *Chem. Mater.* 28 (2016) 7250–7256, <https://doi.org/10.1021/acs.chemmater.6b02002>.
- [16] X. Yu, S.F. Ng, L.K. Putri, L.L. Tan, A.R. Mohamed, W.J. Ong, Point-defect engineering: leveraging imperfections in graphitic carbon nitride (g-C₃N₄) photocatalysts toward artificial photosynthesis, *Small* 17 (2021) 1–45, <https://doi.org/10.1002/sml.202006851>.
- [17] G. Liu, P. Niu, C. Sun, S.C. Smith, Z. Chen, G.Q. Lu, H.M. Cheng, Unique electronic structure induced high photoreactivity of sulfur-doped graphitic C₃N₄, *J. Am. Chem. Soc.* 132 (2010) 11642–11648, <https://doi.org/10.1021/ja103798k>.
- [18] A. Kumar, V. Krishnan, Vacancy engineering in semiconductor photocatalysts: implications in hydrogen evolution and nitrogen fixation applications, *Adv. Funct. Mater.* 31 (2021) 1–34, <https://doi.org/10.1002/adfm.202009807>.
- [19] P. Niu, L. Zhang, G. Liu, H.M. Cheng, Graphene-like carbon nitride nanosheets for improved photocatalytic activities, *Adv. Funct. Mater.* 22 (2012) 4763–4770, <https://doi.org/10.1002/adfm.201200922>.
- [20] J. Xu, L. Zhang, R. Shi, Y. Zhu, Chemical exfoliation of graphitic carbon nitride for efficient heterogeneous photocatalysis, *J. Mater. Chem. A* 1 (2013) 14766–14772, <https://doi.org/10.1039/c3ta13188b>.
- [21] S. Yang, Y. Gong, J. Zhang, L. Zhan, L. Ma, Z. Fang, R. Vajtai, X. Wang, P. M. Ajayan, Exfoliated graphitic carbon nitride nanosheets as efficient catalysts for hydrogen evolution under visible light, *Adv. Mater.* 25 (2013) 2452, <https://doi.org/10.1002/adma.201204453>.
- [22] W. Iqbal, B. Qiu, Q. Zhu, M. Xing, J. Zhang, Self-modified breaking hydrogen bonds to highly crystalline graphitic carbon nitrides nanosheets for drastically enhanced hydrogen production, *Appl. Catal. B Environ.* 232 (2018) 306–313, <https://doi.org/10.1016/j.apcatb.2018.03.072>.
- [23] I. Papailias, N. Todorova, T. Giannakopoulou, N. Ioannidis, N. Boukos, C. P. Athanasekou, D. Dimotikali, C. Trapalis, Chemical vs thermal exfoliation of G-C₃N₄ for NO_x removal under visible light irradiation, *Appl. Catal. B Environ.* 239 (2018) 16–26, <https://doi.org/10.1016/j.apcatb.2018.07.078>.
- [24] Q. Lin, L. Li, S. Liang, M. Liu, J. Bi, L. Wu, Efficient synthesis of monolayer carbon nitride 2D nanosheet with tunable concentration and enhanced visible-light photocatalytic activities, *Appl. Catal. B Environ.* 163 (2015) 135–142, <https://doi.org/10.1016/j.apcatb.2014.07.053>.
- [25] K. Maeda, Z-scheme water splitting using two different semiconductor photocatalysts, *ACS Catal.* 3 (2013) 1486–1503, <https://doi.org/10.1021/cs4002089>.
- [26] P. Zhou, J. Yu, M. Jaroniec, All-solid-state Z-scheme photocatalytic systems, *Adv. Mater.* 26 (2014) 4920–4935, <https://doi.org/10.1002/adma.201400288>.
- [27] V.W.H. Lau, I. Moudrakovski, T. Botari, S. Weinberger, M.B. Mesch, V. Duppel, J. Senker, V. Blum, B.V. Lotsch, Rational design of carbon nitride photocatalysts by identification of cyanamide defects as catalytically relevant sites, *Nat. Commun.* 7 (2016), <https://doi.org/10.1038/ncomms12165>.
- [28] Y.J. Yuan, Z. Shen, S. Wu, Y. Su, L. Pei, Z. Ji, M. Ding, W. Bai, Y. Chen, Z.T. Yu, Z. Zou, Liquid exfoliation of G-C₃N₄ nanosheets to construct 2D–2D MoS₂/g-C₃N₄ photocatalyst for enhanced photocatalytic H₂ production activity, *Appl. Catal. B Environ.* 246 (2019) 120–128, <https://doi.org/10.1016/j.apcatb.2019.01.043>.
- [29] J. Yuan, X. Liu, Y. Tang, Y. Zeng, L. Wang, S. Zhang, T. Cai, Y. Liu, S. Luo, Y. Pei, C. Liu, Positioning cyanamide defects in g-C₃N₄: engineering energy levels and active sites for superior photocatalytic hydrogen evolution, *Appl. Catal. B Environ.* 237 (2018) 24–31, <https://doi.org/10.1016/j.apcatb.2018.05.064>.
- [30] F. Yu, Z. Wang, S. Zhang, H. Ye, K. Kong, X. Gong, J. Hua, H. Tian, Molecular engineering of donor-acceptor conjugated polymer/g-C₃N₄ heterostructures for significantly enhanced hydrogen evolution under visible-light irradiation, *Adv. Funct. Mater.* 28 (2018) 1–13, <https://doi.org/10.1002/adfm.201804512>.
- [31] W. Wang, X. Bai, Q. Ci, L. Du, X. Ren, D.L. Phillips, Near-field drives long-lived shallow trapping of polymeric C₃N₄ for efficient photocatalytic hydrogen evolution, *Adv. Funct. Mater.* 31 (2021), <https://doi.org/10.1002/adfm.202103978>.
- [32] X. Zhou, B. Jin, L. Li, F. Peng, H. Wang, H. Yu, Y. Fang, A carbon nitride/TiO₂ 2D nanotube array heterojunction visible-light photocatalyst: synthesis, characterization, and photoelectrochemical properties, *J. Mater. Chem.* 22 (2012) 17900–17905, <https://doi.org/10.1039/c2jm32686h>.
- [33] C. Yang, Z. Xue, J. Qin, M. Sawangphruk, X. Zhang, R. Liu, Heterogeneous structural defects to prompt charge shuttle in g-C₃N₄ plane for boosting visible-light photocatalytic activity, *Appl. Catal. B Environ.* 259 (2019), 118094, <https://doi.org/10.1016/j.apcatb.2019.118094>.
- [34] S. Mondal, L. Sahoo, Y. Vaishnav, S. Mishra, R.S. Roy, C.P. Vinod, A.K. De, U. K. Gautam, Wavelength dependent luminescence decay kinetics in “quantum-confined” g-C₃N₄ nanosheets exhibiting high photocatalytic efficiency upon plasmonic coupling, *J. Mater. Chem. A* 8 (2020) 20581–20592, <https://doi.org/10.1039/d0ta08001b>.
- [35] X. Zhang, X. Xie, H. Wang, J. Zhang, B. Pan, Y. Xie, Enhanced photoresponsive ultrathin graphitic-phase C₃N₄ nanosheets for bioimaging, *J. Am. Chem. Soc.* 135 (2013) 18–21, <https://doi.org/10.1021/ja308249k>.
- [36] S. Mishra, D. Takhellambam, A.K. De, D. Jana, Stable CsPbI₃-mesoporous alumina composite thin film at ambient condition: preparation, characterization, and study of ultrafast charge-transfer dynamics, *J. Phys. Chem. C* 125 (2021) 3285–3294, <https://doi.org/10.1021/acs.jpcc.0c10260>.
- [37] A.K. De, S. Satapathi, N.K. Tailor, S. Mishra, T. Sharma, Cation-dependent hot carrier cooling in the lead-free bismuth halide a₃bi₂i₉ (a = fa, ma, and cs) perovskite, *J. Phys. Chem. C* 125 (2021) 9891–9898, <https://doi.org/10.1021/acs.jpcc.1c01509>.
- [38] I.H.M.V. Stokkum, D.S. Lorsche, R.V. Grondella, Global and target analysis of time-resolved spectra, *Biochim. Et Biophys. Acta* 1657 (2004) 82–104, <https://doi.org/10.1016/j.bbabi.2004.04.011>.
- [39] Y. Zheng, Y. Jiao, Y. Zhu, L.H. Li, Y. Han, Y. Chen, A. Du, M. Jaroniec, S.Z. Qiao, Hydrogen evolution by a metal-free electrocatalyst, *Nat. Commun.* 5 (2014) 2–9, <https://doi.org/10.1038/ncomms4783>.
- [40] S. Cao, J. Low, J. Yu, M. Jaroniec, Polymeric photocatalysts based on graphitic carbon nitride, *Adv. Mater.* 27 (2015) 2150–2176, <https://doi.org/10.1002/adma.201500033>.
- [41] Y. Kang, Y. Yang, L.C. Yin, X. Kang, L. Wang, G. Liu, H.M. Cheng, Selective breaking of hydrogen bonds of layered carbon nitride for visible light photocatalysis, *Adv. Mater.* 28 (2016) 6471–6477, <https://doi.org/10.1002/adma.201601567>.
- [42] R. Garg, L. Sahoo, K. Kaur, C.P. Vinod, U.K. Gautam, Single-step insertion of M-Nx moieties in commercial carbon for sustainable bifunctional electrocatalysis: mapping insertion capacity, mass loss, and carbon reconstruction, *Carbon* 196 (2022) 1001–1011, <https://doi.org/10.1016/j.carbon.2022.06.008>.
- [43] J. Li, B. Shen, Z. Hong, B. Lin, B. Gao, Y. Chen, A facile approach to synthesize novel oxygen-doped g-C₃N₄ with superior visible-light photoreactivity, *Chem. Commun.* 48 (2012) 12017–12019, <https://doi.org/10.1039/c2cc35862j>.
- [44] J.W. Zhang, S. Gong, N. Mahmood, L. Pan, X. Zhang, J.J. Zou, Oxygen-doped nanoporous carbon nitride via water-based homogeneous supramolecular assembly for photocatalytic hydrogen evolution, *Appl. Catal. B Environ.* 221 (2018) 9–16, <https://doi.org/10.1016/j.apcatb.2017.09.003>.

- [45] L. Jiang, X. Yuan, G. Zeng, J. Liang, Z. Wu, H. Yu, D. Mo, H. Wang, Z. Xiao, C. Zhou, Nitrogen self-doped g-C₃N₄ nanosheets with tunable band structures for enhanced photocatalytic tetracycline degradation, *J. Colloid Interface Sci.* 536 (2019) 17–29, <https://doi.org/10.1016/j.jcis.2018.10.033>.
- [46] G. Zhang, A. Savateev, Y. Zhao, L. Li, M. Antonietti, Advancing the $n \rightarrow \pi^*$ electron transition of carbon nitride nanotubes for H₂ photosynthesis, *J. Mater. Chem. A* 5 (2017) 12723–12728, <https://doi.org/10.1039/c7ta03777e>.
- [47] M. Li, L. Zhang, X. Fan, Y. Zhou, M. Wu, J. Shi, Highly selective CO₂ photoreduction to CO over g-C₃N₄/Bi₂WO₆ composites under visible light, *J. Mater. Chem. A* 3 (2015) 5189–5196, <https://doi.org/10.1039/c4ta06295g>.
- [48] D. Vidyasagar, S.G. Ghugal, S.S. Umare, M. Banavoth, Extended π -conjugative n-p type homostructural graphitic carbon nitride for photodegradation and charge-storage applications, *Sci. Rep.* 9 (2019) 1–10, <https://doi.org/10.1038/s41598-019-43312-5>.
- [49] H. Tran Huu, M.D.N. Thi, V.P. Nguyen, L.N. Thi, T.T.T. Phan, Q.D. Hoang, H. H. Luc, S.J. Kim, V. Vo, One-pot synthesis of S-scheme MoS₂/g-C₃N₄ heterojunction as effective visible light photocatalyst, *Sci. Rep.* 11 (2021) 1–12, <https://doi.org/10.1038/s41598-021-94129-0>.
- [50] S. Patnaik, D.P. Sahoo, K. Parida, An overview on Ag modified g-C₃N₄ based nanostructured materials for energy and environmental applications, *Renew. Sustain. Energy Rev.* 82 (2018) 1297–1312, <https://doi.org/10.1016/j.rser.2017.09.026>.
- [51] G. Dong, K. Zhao, L. Zhang, Carbon self-doping induced high electronic conductivity and photoreactivity of g-C₃N₄, *Chem. Commun.* 48 (2012) 6178–6180, <https://doi.org/10.1039/c2cc32181e>.
- [52] J. Fang, H. Fan, M. Li, C. Long, Nitrogen self-doped graphitic carbon nitride as efficient visible light photocatalyst for hydrogen evolution, *J. Mater. Chem. A* 3 (2015) 13819–13826, <https://doi.org/10.1039/c5ta02257f>.
- [53] R. Godin, Y. Wang, M.A. Zwiijnenburg, J. Tang, J.R. Durrant, Time-resolved spectroscopic investigation of charge trapping in carbon nitrides photocatalysts for hydrogen generation, *J. Am. Chem. Soc.* 139 (2017) 5216–5224, <https://doi.org/10.1021/jacs.7b01547>.
- [54] E.K. Vishnu, A.A. Kumar Nair, K.G. Thomas, Core-size-dependent trapping and detrapping dynamics in CdSe/CdS/ZnS quantum dots, *J. Phys. Chem. C* 125 (2021) 25706–25716, <https://doi.org/10.1021/acs.jpcc.1c08137>.
- [55] L. Li, E.A. Carter, Defect-mediated charge-carrier trapping and nonradiative recombination in WSe₂ monolayers, *J. Am. Chem. Soc.* 141 (2019) 10451–10461, <https://doi.org/10.1021/jacs.9b04663>.
- [56] K. Zheng, K. Židek, M. Abdellah, J. Chen, P. Chábera, W. Zhang, M.J. Al-Marri, T. Pullerits, High excitation intensity opens a new trapping channel in organic-inorganic hybrid perovskite nanoparticles, *ACS Energy Lett.* 1 (2016) 1154–1161, <https://doi.org/10.1021/acsenergylett.6b00352>.